# Parallel Frameworks for Robust Optimization of Medium Frequency Transformers

Kristen Booth, *Member, IEEE,* Harish Subramanyan, Jun Liu, and Srdjan Lukic, *Member, IEEE*

***Abstract*—Current optimization methods for Medium Frequency Transformers (MFTs) within power electronic converters yield unrealistic results in the multiphysics framework. Comparing the optimal design to an experimental setup for a $3.5\,\mathrm{kW}$ MFT, the core loss is underestimated by 28%, which results in the experimental steady-state temperatures being $10\,^{\circ}\mathrm{C}$ greater than the analytically optimized model. To counteract these disadvantages, an optimization procedure, using the Aggressive Space Mapping (ASM) technique, is experimentally verified and compared to the previous State of the Art (SOA) method. It is shown that the ASM design produces more realistic and feasible experimental outcomes than the SOA design. The core losses are accurately predicted to within 10%, which in turn, vastly improves the thermal modeling accuracy. The ASM method accurately predicts the core hot spot temperature and the average core temperature. This work also introduces a robust optimization method to the MFT design process to handle variations from both converter-level attributes and manufacturing tolerances to create a potential design region which contains 97.725% of possible design outcomes. This method replaces the nominal design optimization that is used to produce the optimized MFTs in the SOA and ASM methods.**

## I. Introduction

MEDIUM Frequency Transformers (MFTs) are vital components of galvanically isolated converters. These transformers are used in a variety of applications, such as Solid State Transformers [1]–[6], Power Electronics Transformers (PETs) [7], [8], and EV fast chargers [9]–[11]. There are two main design considerations, leakage inductance and power density, that constrain MFT implementation when utilized within these converter systems. A tuned leakage inductance enables soft switching for many converters using resonant tanks and aids in power transfer for Dual Active Bridge (DAB) converters. Therefore, the motivation for designing a transformer from the leakage inductance requirements is readily apparent [12], [13]. Optimization processes enable increased converter efficiencies and power densities by tuning the leakage inductance for soft switching and sweeping a switching frequency range for best performance [14].

While the leakage inductance has been the forefront of research in MFT optimization, power density is generally defined as an objective in the optimization process. Notably, the key constraint of power density, thermal dissipation, is modeled yet the implications of a poor thermal design are often overlooked. For example, the experimental steady-state temperatures found in [15] were approximately $20\,^{\circ}\mathrm{C}$ warmer than suggested by the analytical model and FEA. This temperature difference was located at a cooler site of the transformer core, and the effects of this are only exacerbated in hot spot locations, such as the center core limb.

There are several search techniques for multiobjective optimization. The most popular in transformer optimization are brute force methods and genetic algorithms [13], [16]–[21]. When converting these simulated, optimized designs to experimental hardware, there is a large mismatch between the expected outcomes and the experimental results. This negatively impacts the potential of MFT optimization since there is currently no advantage to using optimization on MFTs. By incorporating model-to-hardware mapping and calculating the parametric uncertainties, MFT optimization procedures have the potential to achieve greater usage.

Overall, it can be seen that discrepancies between MFT models and experimentation exist. The literature has attempted to reduce this error by implementing Space Mapping algorithms for previous MFT designs using analytical and FEA models [22]–[24]. However, these works proposed minutely modifying core dimensions to improve the design [22], [23]. This is not feasible with commercially available core shapes which forces these discussions to remain theoretical. In this proposed method, an analytical model and experimental hardware are conjointly implemented to create feasible, realistic design changes. The proof for the usefulness of this technique is provided in [24]. Space mapping created a dominating Pareto front when compared to an efficient global optimization routine. Space mapping techniques have also been used for designing electrical machines as a method to reduce computational effort while increasing accuracy [25]–[27].

It is important to note the assets and requirements of space mapping techniques. The advantages lie in the ease of implementation and reduction of computational effort. When space mapping was compared to a 3-D FEA optimization routine in [27], the space mapping technique converged within 15% of the time needed for the FEA. However, a space mapping approach assumes the existence of two models: a fast, less accurate model and a more intensive, high accuracy model. The faster model must also maintain a similar trend to the accurate model for efficient implementation of space mapping.

The purpose of this work is twofold: (i) to reduce the error between the analytical and experimental results and (ii) to understand the parametric uncertainties in MFT optimization. The discrepancies between the modeled and physical realms is caused by model assumptions. Using a technique called Aggressive Space Mapping (ASM), the MFT optimization is

This material is based upon work supported by the National Science Foundation under Grant No. DGE-1252376 and Grant No. 1827714.

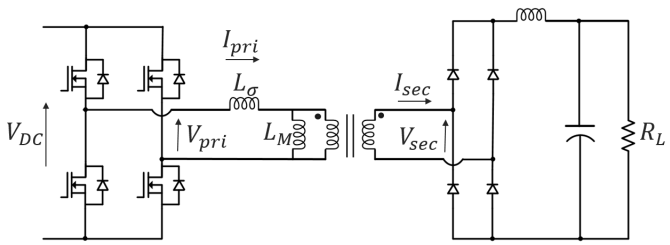


Fig. 1. Single-active bridge DC-DC converter used in MFT testing.

TABLE I
TRANSFORMER DESIGN REQUIREMENTS

| | Specification | Rating or Range |
|---|---|---|
| Design Specifications | Primary Voltage, $V_{pri}$ | 450 V |
| | Turns Ratio, $N_{\text{ratio}}$ | 1:1 |
| | Rated Power, $P_r$ | 3.5 kW |
| Design Variables | Number of Cores, $N_{\text{core}}$ | 1-10 |
| | Primary Turns, $N_{pri}$ | 2-24 |
| | Switching Frequency, $f_{sw}$ | 25–200 kHz |

modified to reduce the error between the core losses in the analytical and experimental realms. The proposed optimization method uses a formulated mathematical procedure to shift the analytical design and the physical implementation results into agreement. This algorithm is advantageous for small-scale production of MFTs for various applications, but it does not aid design for large-scale manufacturing nor encourage a deep understanding of design variation impacts.

In mass production, infeasible hardware can be created from a feasible, nominally optimized design. This optimized design is susceptible to variation, and infeasibility, due to the active optimization constraints. Infeasible hardware includes any prototype that cannot function at its desired performance due to any specification, such as temperature constraints, being surpassed. Even though space mapping creates accurate mapping from an optimized design point to experimental results, parametric uncertainties cause variation which can impede realization of the design point. Therefore, an optimized design is not adequate; the ideal situation is an optimized design that is *robust* and can tolerate variation. Tolerances are the means to define deviation due to uncertainty in the manufacturing process or system-level attributes.

Robust optimization was originally developed in 1993 to account for these deviations in design [28]. This method was extended to worst-case tolerances which contains all the potential designs in the feasible region [29]. Since the likelihood of all worst-case variances being combined into one design is low, this method would overdesign the MFT and excessively increase its size and reduce its efficiency. A Taguchi-based method that minimizes variation is discussed in [30]; however, this method is inaccurate for highly nonlinear optimization problems, such as MFT optimization. Variations of robust optimization are discussed in detail, and the applications of these methods are given in [31]. For this work, a straight-forward statistical analysis method enables optimization while acknowledging variation in design based on parameter uncertainty [32]. These variations can occur in product manufacturing or changing operating conditions.

This paper is divided into six sections. The design considerations are given in Section II. Section III provides the analytical background into the transformer optimization process. These equations are then used in Section IV to develop the multiobjective optimization algorithms with power density and efficiency as the objectives. Experimental results of the the two nominal optimization methods are also compared. Moving into design regions of robust optimization, Section V defines the methodology and compares these results to the experimental results of the nominal optimization method. Finally, conclusions are discussed in Section VI.

## II. DESIGN CONSIDERATIONS

To implement this transformer optimization algorithm, a simple single-active bridge DC-DC converter, shown in Fig. 1, is used to experimentally verify the transformer losses and steady-state temperatures. The transformer requirements, given in Table I, detail the design specifications and variable ranges for the optimization procedure. As this design is a scaled-down model for grid applications, the rated power is designed such that the experiment can run until the temperature of the MFT reaches steady state. While currently uncommon for SiC MOSFETs to be switched at these higher frequencies, they are capable, and future designs for power electronics may require it. Therefore, the goal of this work is to specifically focus on the most optimal case for MFTs. Future work will implement the trade-offs between the semiconductors and the MFTs. For the design variables, all ranges have been chosen such that there is a large range of potential, feasible designs within the performance space of the optimization procedure. The primary turns are limited by the window area of the core, and the switching frequency spans the frequency range given in the datasheet of the magnetic material. For this design, the leakage inductance consideration is beyond the scope of this work; however, the changes in leakage inductance must be monitored in ASM to ensure a feasible application to a converter with specific requirements.

To avoid designs that cannot be built due to expensive specialty components, the design variables are discrete and can be adjusted using only commercially available components. For this case study, the E-cores are chosen to be TDK N87 ferrite E80/38/20, and the windings are 40 AWG stranded Litz wire that can handle the required current. The frequency can be modified by the microcontroller, TI TMS320F28069M, with high accuracy.

All optimization techniques within this work are multiobjective. The two objectives are power density, $\rho$, and efficiency, $\eta$.

## III. METHODOLOGY

This section describes the transformer characteristic equations used in the optimization routine. These analytical equations are the basis of the fast, less accurate model for use in the Space Mapping approach. While these models need to have a similar trend, and hence moderate accuracy, as the

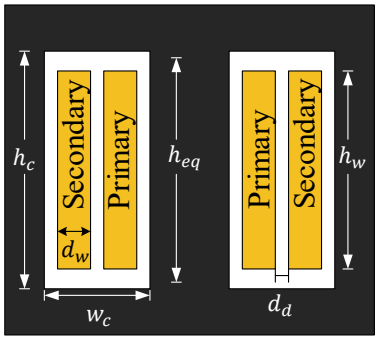


Fig. 2. Physical parameters for leakage inductance calculation.

finer and more computationally taxing model, there is room for assumptions that can aid in the computational speed of the algorithm. The fine model results, in coordination with the mapping procedure, help to overcome the inaccuracies that may develop due to assumptions in the faster model. Fundamental models necessary to the optimized design for MFTs are the leakage inductance, winding and core losses, and steady-state thermal analyses. These analytical models have been previously developed and verified to within a reasonable degree of accuracy by the respective authors as cited. The purpose of this section is to provide the analytical models used for this research. The overview of each analytical model, as previously described in [33], is provided.

### A. Leakage Inductance

The leakage inductance, $L_\sigma$, is calculated using the methods described in [34]. For Litz wire, the porosity factor can be calculated as

$$\eta = \frac{N_{sv} d_{eq}}{h_{core}} \tag{1}$$

where $d_{eq} = \sqrt{\frac{\pi}{4}} d_r$ and $h_{core}$ is the height of the core. Addressing the nonuniform structure of Litz winding, the number of strands within the Litz wire oriented horizontally, $N_{sh}$, or vertically, $N_{sv}$, can be calculated as

$$N_{sh} = \sqrt{\frac{N_s}{K_w}} \text{ and} \tag{2}$$

$$N_{sv} = \sqrt{K_w N_s} \tag{3}$$

where the assumed proportional total winding cross-sectional profile is given as

$$K_w = \frac{h_w}{d_{eq}}. \tag{4}$$

The Rogowski factor adjusts the equivalent length of the magnetic flux and is found by

$$K_R = 1 - \frac{1 - e^{-\pi h_w/(d_{w,pri} + d_d + d_{w,sec})}}{\pi h_w/(d_{w,pri} + d_d + d_{w,sec})} \tag{5}$$

which creates the improved height,

$$h_{eq} = \frac{h_w}{K_R}, \tag{6}$$

as shown in Fig. 2.

Therefore, the modified Dowell's method to include these modifications is

$$\begin{aligned} L_\sigma = &\mu_0 N_{pri}^2 \frac{MLT}{h_{eq}} \left[ \frac{d_{eq,pri} N_{sh}}{3} F_{w,pri} + \frac{d_{eq,sec} N_{sh}}{3} F_{w,sec} \right. \\ &+ d_d + d_{wi,pri} \frac{(N_{sh}-1)(2N_{sh}-1)}{6N_{sh}} \\ &\left. + d_{wi,sec} \frac{(N_{sh}-1)(2N_{sh}-1)}{6N_{sh}} \right] \end{aligned} \tag{7}$$

where

$$F_{w,y} = \frac{1}{2N_{sh}^2 \Delta} \left[ (4N_{sh}^2 - 1)\varphi_1 - 2(N_{sh}^2 - 1)\varphi_2 \right], \tag{8}$$

$$\varphi_1 = \frac{\sinh(2\Delta) - \sin(2\Delta)}{\cosh(2\Delta) - \cos(2\Delta)}, \tag{9}$$

$$\varphi_2 = \frac{\sinh(\Delta) - \sin(\Delta)}{\cosh(\Delta) - \cos(\Delta)}, \tag{10}$$

$$\delta = \sqrt{\frac{1}{\pi \mu_0 \eta \sigma f_{sw}}}, \tag{11}$$

$N_{pri}$ is the number of primary winding turns, $MLT$ is the mean length per turn, $\Delta = \frac{d_{eq}}{\delta}$, $d_d$ is the gap between the primary and secondary windings, $d_{w,y}$ is the equivalent winding width, $d_{wi,y}$ is the width of the dielectric between layers, $\sigma$ is the conductivity of the conductor, and $f_{sw}$ is the switching frequency.

### B. Winding Losses

Winding losses are comprised of two facets: skin effect and proximity losses. These two loss components can be assumed to be orthogonal for a model containing a symmetric conductor about its axes in its cross-sectional area [17]. Therefore,

$$P_{cu} = P_{AC} + P_d \tag{12}$$

where $P_{cu}$ is the total winding loss, $P_{AC}$ is the winding losses due to skin effect as calculated by AC resistance, $R_{AC}$, and $P_d$ is defined as proximity losses.

Using the manufacturer's method for winding resistance due to the skin effect as described in [35], the winding losses for Litz wire can be determined using

$$R_{DC} = \frac{R_s (1.015)^{N_B} (1.025)^{N_C}}{N_S} \tag{13}$$

and

$$R_{AC} = \left[ H + K \left( \frac{N_S \times D_I}{D_O} \right)^2 G \right] R_{DC}. \tag{14}$$

$R_{DC}$ is DC resistance [$\Omega$/1000 ft], $R_S$ is the maximum DC resistance, $N_B$ is the bunching operations number, $N_C$ is the cabling operations number, and $N_S$ is the number of individual strands. $R_{AC}$ is AC resistance [$\Omega$/1000 ft], $D_I$ is the individual strand diameter [in], and $D_O$ is entire cable diameter [in]. $H$ and $K$ are given by the manufacturer, and $G = \left( \frac{D_I \sqrt{f * 1000}}{10.44} \right)^4$.

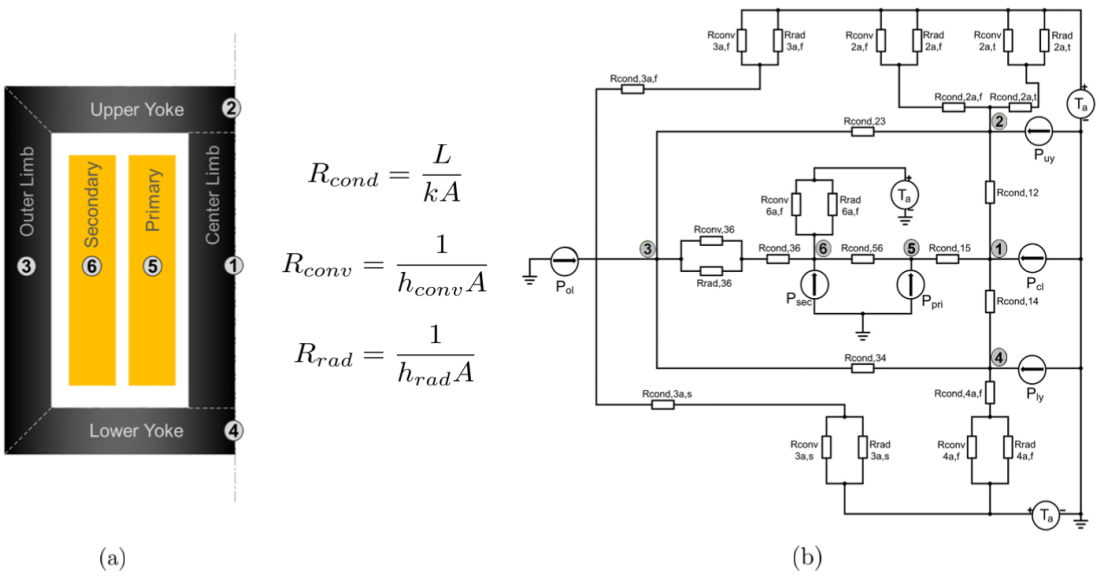


(a) (b)

Fig. 3. (a) Two-dimensional MFT structure with nodal temperature locations. (b) Thermal resistive network for MFT design [33].

Then, the proximity losses can be calculated by a simplified Dowell's method [36] using

$$P_d = h_w \sum_{i=0}^{N} \frac{MLT_i H_i^2}{d_{w,i}\sigma}\left[(1+\nu_i^2)G_1(\Delta_i) - 4\nu_i G_2(\Delta_i)\right] \quad (15)$$

where $N$ is the number of winding layers, $H_i$ is the magnetic field at the $i$th layer, $\nu$ is the ratio of magnetic fields on either side of layer $i$,

$$G_1(\Delta) = \Delta\frac{\sinh(2\Delta)+\sin(2\Delta)}{\cosh(2\Delta)-\cos(2\Delta)}, \text{and} \quad (16)$$

$$G_2(\Delta) = \Delta\frac{\sinh(\Delta)\cos(\Delta)+\cosh(\Delta)\sin(\Delta)}{\cosh(2\Delta)-\cos(2\Delta)} \quad (17)$$

as defined in [37].

### C. Core Losses

The improved General Steinmetz Equation (iGSE) is most commonly used to calculated core losses for MFT optimization algorithms [38]. iGSE is defined as

$$P_c = \frac{1}{T}\int_0^T k_i \left|\frac{dB(t)}{dt}\right|^{\alpha} (\Delta B)^{\beta-\alpha} dt \quad (18)$$

where

$$k_i = \frac{K}{(2\pi)^{\alpha-1}\int_0^{2\pi} |\cos\theta|^{\alpha} 2^{\beta-\alpha} d\theta}, \quad (19)$$

$K$, $\alpha$, and $\beta$ are given by the manufacturer [39]. iGSE is the most widely used core loss empirical method for MFTs as it reduces to a simple equation for square wave excitation found in MF converters. These coefficients are found using a loss map, generated from manufacturer information, which is dependent on the switching frequency, flux density, and temperature. Since $K$, $\alpha$, and $\beta$ are dependent on the core temperature, an iterative process between the core losses and thermal steady-state calculations occurs until equilibrium is reached.

### D. Power Density

The volume of the MFT is calculated in two parts: (i) the volume of the cores, including the free space in the window, and (ii) the winding outside the window area of the core. The volume of the cores is defined as

$$V_{\text{core}} = N_{\text{core}} \times L_{\text{core}} \times W_{\text{core}} \times H_{\text{core}} \quad (20)$$

where $N_{\text{core}}$ is the number of core sets, $L_{\text{core}}$ is the length of the core, $W_{\text{core}}$ is the width of the core on the window side, and $H_{\text{core}}$ is the height of a full core set.

The winding volume, outside the core volume, for each winding is calculated as

$$V_{\text{w}} = (MLT - 2N_{\text{core}}L_{\text{core}})\, A_c. \quad (21)$$

Finally, the power density is given as

$$\rho = \frac{P_r}{V_{\text{core}} + V_{\text{w, pri}} + V_{\text{w,sec}}} \quad (22)$$

where $P_r$ is the rated power of the MFT.

### E. Thermal modeling

A 2-D analytical thermal model is employed to estimate the temperatures of the core and windings, a simplified version of which can be found in [15]. It was first validated using steady-state thermal FEA in ANSYS in order to confirm the hot spot locations and verified using experimental results on a selected transformer design that was built prior to the optimized MFT hardware in this study.

In order to calculate the average temperature of the core, it is divided into four zones: center limb, upper yoke, lower yoke, and outer limb, as shown in Fig. 3(a). The core losses are assumed to be uniformly distributed across these four zones

as internal heat generation sources which are directly proportional to the volume of the corresponding zone. Similarly, the primary and secondary winding losses are modeled as heat sources.

The heat is transferred across the different core zones and the windings by conduction. Convection and radiation pathways are responsible for loss of heat from the sides and top of the core [15], [40]. The bottom surface is assumed to be perfectly insulated to emulate extreme conditions. The heat is exchanged between the windings and the core by conduction across the contact surface. The model also incorporates convection in the core window into the temperature calculations. It was observed that heat transfer within the core window played a critical role in determining the temperature of the windings accurately.

The well-known electrical circuit analogy is used to couple the heat transfer across the core and windings where different heat transfer mechanisms are characterized by thermal resistances. A detailed resistance network is shown in Fig. 3(b). The admittance matrix, $\mathbf{Y}$, was derived using the six nodal points which were selected to best reflect the temperature profile across the transformer. The temperatures at the respective nodes can be obtained using

$$\mathbf{Q} = \mathbf{Y}\Delta\mathbf{T} \tag{23}$$

where $\mathbf{Q}$ is the heat loss and $\Delta\mathbf{T}$ is the temperature matrix. Nodes 1, the center core limb, and 5, the primary winding, are expected to be the hot spots for the core and winding respectively due to the nature of their locations in the resistance network and the power loss generated by the individual components of the MFT.

The steady-state thermal module in ANSYS Workbench was used to verify the analytical model temperatures, and thereby, the core and winding losses. A 3-D model of the transformer was constructed, identical to the experimental setup with the assumption that the windings can be modeled as a rectangular volume that encompasses the center limb. The losses were modeled as internal heat generation sources across the core and windings. Radiation transfer was defined across all winding surfaces and view factors were incorporated into the calculations to avoid overestimation of winding temperatures. Furthermore, temperature dependent heat transfer coefficients were specified for all convection calculations. To improve the accuracy of the model and replicate the test conditions as closely as possible, the heat transfer in the air interface between the windings and core were represented by defining a manual contact in ANSYS. The thermal resistance of air was input into the formulation to emulate the thermal conductance between the contact surfaces [41], [42]. To ensure the accuracy of the FEA model, a random nonoptimal MFT design was experimentally tested, and real-time effects were incorporated into the FEA model.

### *F. Experimental Measurements*

To compare the optimization techniques, a $3.5\,\mathrm{kW}$ MFT is optimized and verified via experimentation. Three separate tests enable full transformer characterization. The first test

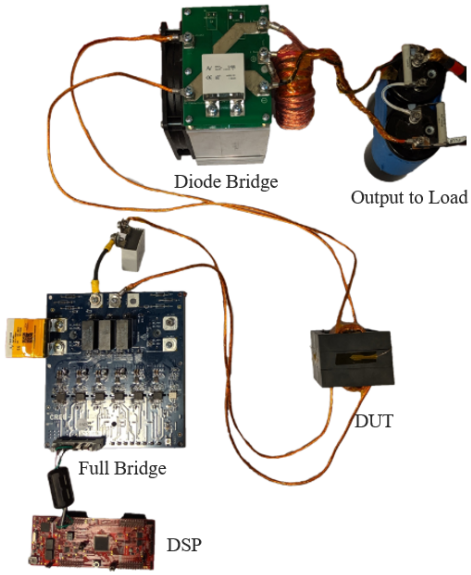


Fig. 4. Experimental setup for full load test.

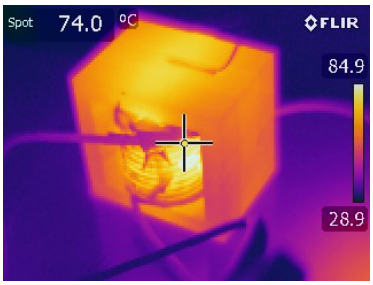


Fig. 5. Infrared imaging used during MFT testing.

involves allowing the fully-loaded transformer setup, shown in Fig. 4, to run until steady-state temperature is reached. The DSP sends the gating signals to the full bridge which is then connected to the transformer. The increased MFT winding length enables thermal isolation from the rest of the converter as assumed by the thermal model and allows the MFT under test to be placed in the thermal chamber for core loss measurements. The secondary side is connected to a diode bridge which is loaded to achieve nominal power. Since the scope of this research does not include full converter efficiency, losses outside the MFT are not considered. The temperatures were measured using thermocouples mounted on the MFT at the strategic nodes from Fig. 3. The data was then collected and recorded via a thermal DAQ. The steady-state condition metric was a temperature change of less than $1\,^{\circ}\mathrm{C}$ every $15\,\mathrm{min}$ for the selected nodes. An infrared camera was also used to monitor the temperature profile, as shown in Fig. 5, but it is important to note that the camera cannot provide thermal data internal to the transformer, such as at the center limb or primary winding.

Due to the temperature-loss relationship, the core losses are measured at the average core temperature produced in the first measurement. This is accomplished by heating the device in a thermal chamber and reproducing the voltage waveform, hence

the flux density, to recreate the core losses at the specified temperature as shown in Fig. 6. Two key assumptions of this test include that the temperature of the transformer must be uniform. This test can only be performed after the MFT has been heated for a long period of time. Second, it is important to maintain a temperature as close to the average temperature found in the first test due to the relationship between core loss and temperature. A slight shift in temperature can create misalignment in the core loss measurement.

Finally, the winding losses are measured by shorting the secondary winding of the transformer in Fig. 6. This test does not need to correlate with heating the device. These last two tests allow for separation of the MFT losses for better analysis. All measurements are taken with a Tektronix MDO3034 with a P2500A voltage probe and a TCP312A current probe. The data are then imported to MATLAB for analysis.

## IV. Nominal Optimization of Transformer Design

Using the equations laid out in Section III and the design specifications from Section II, an optimization routine can be implemented based on the generic optimization stated as

$$\begin{aligned} &\text{Min} \quad f(\mathbf{x}) \\ &\text{s.t.} \quad g_i(\mathbf{x}) \leq b_i \quad i = 1, \ldots, m \end{aligned} \tag{24}$$

where $\mathbf{x}$ is an $n$ dimensional vector of design variables, $g_i$ is the $i^{\text{th}}$ constraint with its respective boundary, $b_i$. This optimization problem statement is considered a nominal optimization algorithm. This means that the design is undisturbed by any variation and assumes that nominal inputs and outputs will occur. For this specific case study, (24) is written as

$$\begin{aligned} &\text{Max} f(\mathbf{x}) = \eta(\mathbf{x}) + \rho(\mathbf{x}) \\ &\text{s.t.} \quad 50\,\text{mT} \leq B_m \leq 200\,\text{mT and} \\ &\mathbf{T} = T_{amb} + \Delta\mathbf{T} \leq \mathbf{T}_{max} \end{aligned} \tag{25}$$

where $\eta$ is the MFT efficiency and $\rho$ is the power density.

In this section, two nominal optimization methods are discussed, experimentally tested, and compared. By starting with the SOA method as a baseline, the differences between the optimized design and hardware can be inspected for this 3.5 kW setup. Then, the ASM technique, which relies on the both the analytical model and the results from the SOA, can map the analytical model to the experimental setup to redesign the experimental setup until the experimental results are within a specified tolerance of the analytical estimations.

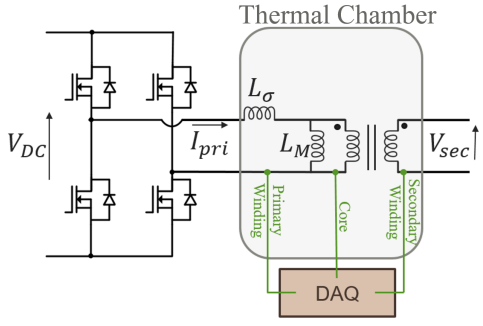


Fig. 6. Core loss measurement method.

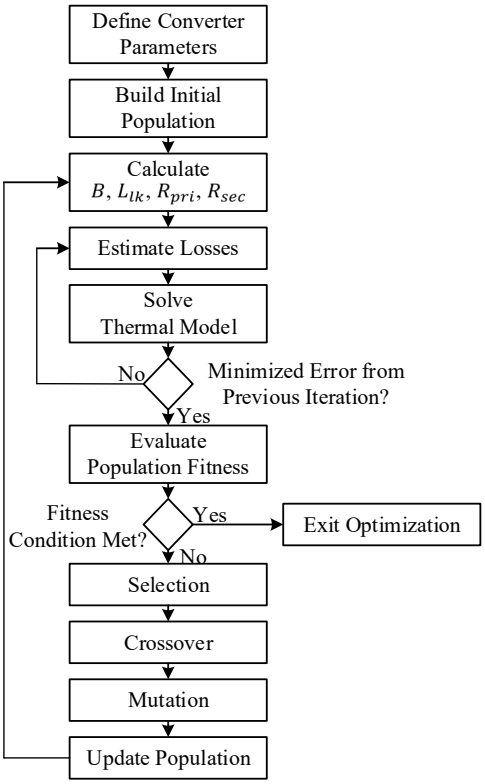


Fig. 7. Nominal optimization routine for MFTs.

### A. State of the Art Method

There are several search techniques for multiobjective optimization. The most popular in transformer optimization are brute force methods [13], [16], [43]. Brute force is known to be computationally expensive based on the mesh scale. This can be improved by refining the mesh closer to desirable designs [43]. Another method in the literature is steepest decent [44]. The disadvantage of steepest descent for MFT optimization is the potential for entrapment in local minima. A local minimum could occur for various core materials, winding structures, and switching frequencies. To overcome this challenge, the initial design estimate must be carefully considered.

This work uses the Natural Selection Genetic Algorithm (NSGA-II) to further reduce computational effort via the MATLAB Optimization Toolbox™ [45]. The optimization objectives are efficiency and power density. The algorithm is detailed in Fig. 7. This method follows the NSGA-II methodology, but the evaluation of the population is shown in detail for this specific application. Due to the highly dependent nature of the total loss and thermal calculations, a second optimization routine is employed within the NSGA-II to minimize the error within the thermal model from the previous calculation for each individual. After all individuals have been evaluated, the population fitness is determined, and NSGA-II proceeds with updating the population for the next generation.

Based on the requirements in Table I, the objective space is shown in Fig. 8. Due to the discrete design variables, the

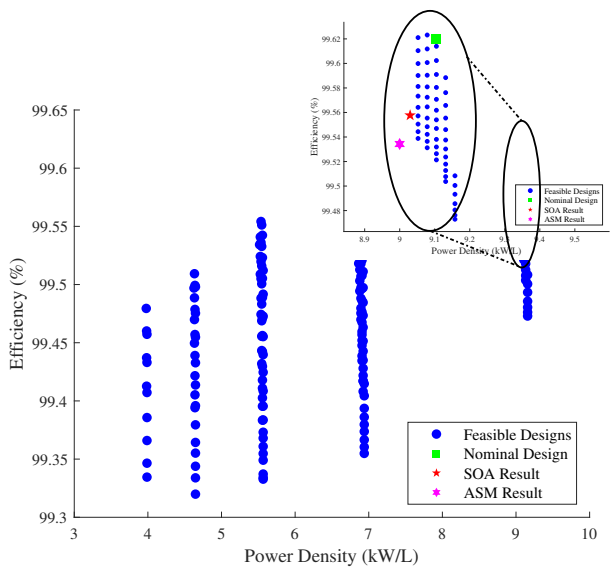


Fig. 8. Objective space of MFT optimization including feasible design (circles), the chosen design (square), and experimental results of SOA (star) and ASM (hexagram).

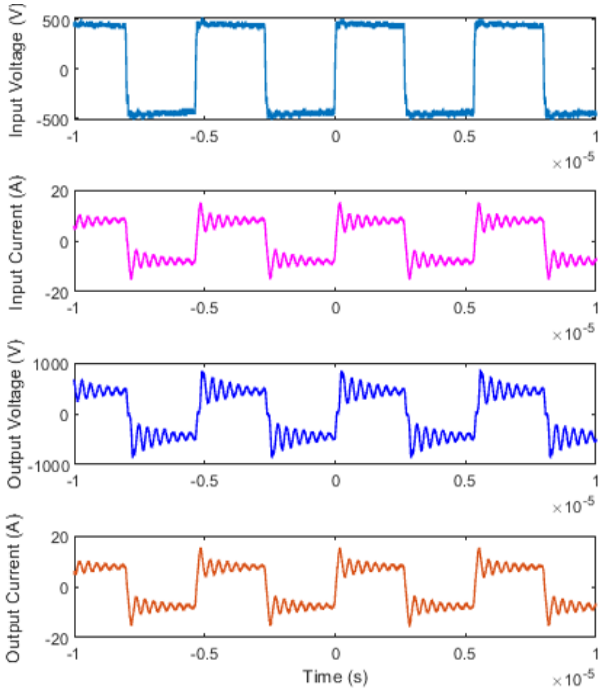


Fig. 9. SOA full load experimental results.

multiobjective optimization has displayed seemingly vertical lines for each change in core size. While it appears as though the two objectives require no trade-offs, there are small variations in the total volume by changing the number of turns, and the Pareto front extends to a 2-core design with an efficiency of 92.55% and a power density of 13.41 kW/L outside the bounds of Fig. 8. These trade-offs are more apparent in previous publications, such as [13], that do not use discrete components, yet these show outcomes that require specialty components with increased cost. The chosen nominal design point for the experimental build has three shell-type cores, 10 turns for each winding, and a switching frequency of 187.5 kHz as the design variables. The projected outcomes for this design are a power density of 9.1 kW/L and an efficiency of 99.62%.

### *B. State of the Art Experimental Results*

To measure the inconsistency between the analytical model and its hardware, the initial experimental design is identical to the chosen nominal design in Section IV-A. The transformer was built using three cores, 10 turns for each winding, and a switching frequency of 187.5 kHz.

The full load test results are found in Fig. 9. The average temperature of the core is 82 °C. The core losses are 7.4 W, and the winding losses are 3.8 W and 4.3 W, respectively. The measured efficiency is 99.56%, and the power density is 9.03 kW/L. This information is summarized for comparison in Section IV-E.

The data from this test shows a 28% difference between the simulated and experimental core losses while the winding losses are accurately depicted by the model. This, in turn, creates a steady-state average core temperature difference of 10 °C. The core hot spot at Node 1 is underestimated by 12.5 °C while the winding temperatures are overestimated. It is concluded that the differences between the analytical model and these experimental results are not compatible.

The FEA thermal model was simulated with the experimental losses, and the temperatures obtained from the experiment are in good agreement, as shown in Fig. 10. The calculated values closely resemble those measured by the thermocouples. The core hot spot is accurately predicted as 97.1 °C. The average temperature of the core from FEA is 88.1 °C. This overestimation can be attributed to the assumption within ANSYS that the bottom surface is perfectly insulated. In real-time conditions, the core was observed to dissipate heat from the bottom surface to the test workbench, which in turn acted

| Nodal temperatures (°C) | | | | | |
|---|---|---|---|---|---|
| (1) Inner | (2) Top | (3) Outer | (4) Bottom | (5) Primary | (6) Secondary |
| 97.1 | 87.7 | 77.4 | 90.5 | 113.8 | 111.1 |

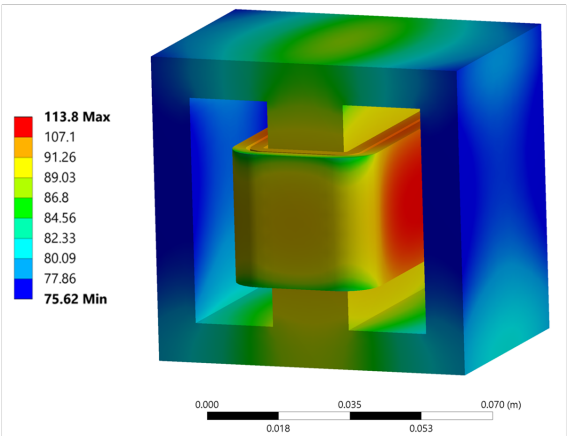


Fig. 10. Thermal FEA model results of SOA design and predicted nodal temperatures.

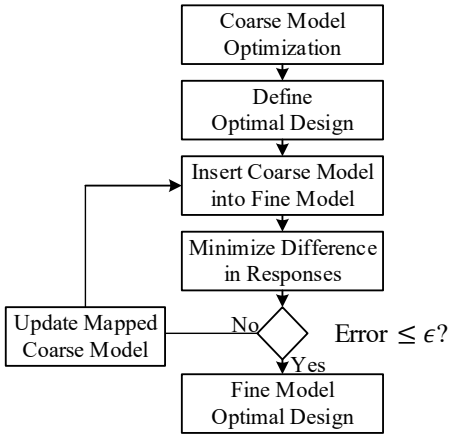


Fig. 11. ASM optimization algorithm for MFTs.

as a heat spreader causing the bottom surface to be cooled. The nodal temperatures at all other points are accurately predicted by the FEA model within a 5% margin of error.

### C. Aggressive Space Mapping Method

With the discrepancies between the optimization algorithm and the experimental results due to modeling error, the next logical step is to reduce the error. Therefore, ASM is used to counteract these disadvantages. The flow chart of ASM is shown in Fig. 11. Since ASM requires a unique solution to converge, the core losses for the NSGA-II optimal design and experimental results are employed as the initial step for ASM. Using the total losses or one of the final objectives would cause the algorithm to fail due to this requirement.

Utilizing the design point chosen in the previous subsection, ASM can be realized using the analytical results and experimental data from the previous two subsections. In this work, the coarse model is the NSGA-II approach. This method enables a fast design space exploration to report potential designs from the Pareto front. The fine model can be either a more accurate model, such as 3-D FEA, or the physical experiment itself. Since all models have some limitation, the experimental hardware is chosen for the fine model. This eliminates modeling error in the reported outcomes in the final experimental design.

In ASM, a coarse model is calibrated using a fine model. ASM starts with the optimization argument

$$\mathbf{x}^* \triangleq arg\min_{\mathbf{x}^*} U(\mathbf{R}(\mathbf{x})), \tag{26}$$

where $\mathbf{R} \in \mathbb{R}^{m\times 1}$ is a vector of $m$ responses of the model, $\mathbf{x}$ is the vector of $n$ design parameters, and $U$ is the objective function [46], [47]. $\mathbf{x}^*$ is the unique optimal solution to be determined.

The fundamental component of ASM is that the coarse model (analytical model) and fine model (experimental data), $\mathbf{x}_c$ and $\mathbf{x}_f \in \mathbb{R}^{n\times 1}$ respectively, can be mapped, $\mathbf{P}$, as

$$\mathbf{x}_c = \mathbf{P}(\mathbf{x}_f) \tag{27}$$

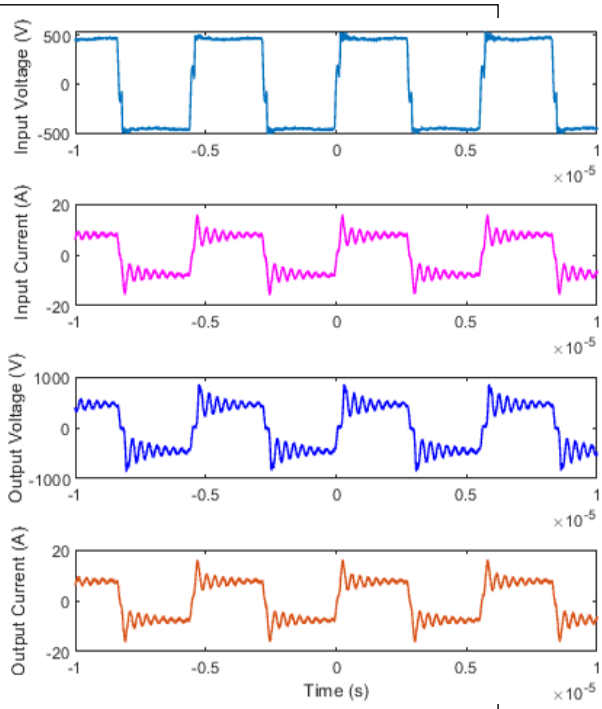


Fig. 12. ASM full load experimental results.

such that

$$\mathbf{R}_c(\mathbf{P}(\mathbf{x}_f)) \approx \mathbf{R}_f(\mathbf{x}_f) \tag{28}$$

in a region of interest where $\mathbf{R}_c$ and $\mathbf{R}_f \in \mathbb{R}^{m\times 1}$ are the corresponding response vectors. This means that the coarse model can be mapped to the fine model through the parameter extraction, $\mathbf{P}$, in some small region near $\mathbf{x}^*$. In this case, $\mathbf{x}_c$ is the chosen NSGA-II nominal optimal point from Section IV-A in Fig. 8.

By reducing the error of this mapping, the optimal result in the fine model is reached. As $\mathbf{R}_f(\mathbf{x}_f^{j+1})$ goes to $\mathbf{R}_c(\mathbf{x}_c)$, then $\mathbf{x}_c^{j+1} = \mathbf{P}(\mathbf{x}_f^{j+1})$ approaches $\mathbf{x}_c^*$ as the iteration number reaches a final converging iteration, $M$,

$$||\mathbf{x}_c^{j+1} - \mathbf{x}_c^*|| \leq \epsilon \quad as\ j \to M \tag{29}$$

where $\epsilon$ is a set tolerance. As the iterations occur to improve the mapping, this creates a set of $n$ nonlinear equations,

$$\mathbf{f}(\mathbf{x}_f) = \mathbf{P}(\mathbf{x}_f) - \mathbf{x}_c^* = \epsilon \tag{30}$$

where $\mathbf{f}$ is called the residual vector. This is used to create the change for the fine model updates.

Let $\mathbf{x}_f^{(j)}$ be the $j$th iteration to the solution of (30) and $\mathbf{f}^{(j)}$ stand for $\mathbf{f}(\mathbf{x}_f^{(j)})$. The next iteration can be found by a quasi-Newton method

$$\mathbf{x}_f^{(j+1)} = \mathbf{x}_f^{(j)} + \mathbf{h}^{(j)} \tag{31}$$

where $\mathbf{h}$ is the solution to

$$\mathbf{B}^{(j)}\mathbf{h}^{(j)} = -\mathbf{f}^{(j)}, \tag{32}$$

and $\mathbf{B}$ is an approximation to the Jacobian matrix. For the first iteration, $\mathbf{B}^{(1)}$ is the identity matrix. For every iteration

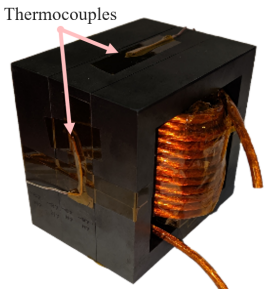


Fig. 13. Physical transformer for the ASM design with thermocouples.

following, $\mathbf{B}$ is updated by the Broyden formula which can be reduced to

$$\mathbf{B}^{(j+1)} = \mathbf{B}^{(j)} + \frac{\mathbf{f}^{(j+1)}\mathbf{h}^{(j)T}}{\mathbf{h}^{(j)T}\mathbf{h}^{(j)}}. \tag{33}$$

The algorithm is complete when

$$||\mathbf{f}^{(j+1)}|| \leq \epsilon. \tag{34}$$

### D. Aggressive Space Mapped Experimental Results

This space mapping method uses the SOA experimental results from Section IV-B to shift the final design build into the core loss and temperature region expected from the simulated results. The parameter extraction to solve for the mapping, $\mathbf{P}$, can be an abstraction. To clarify, the coarse model is swept to find a design point that also has the same core loss of $7.4\,\mathrm{W}$ as the SOA experimental result. Due to the nonlinearity of the system, the sweep is limited to designs that are limited to within $1\%$ of the core loss while being as near to the original design variables as possible. This output is then used in (30)-(32) to choose the new design point. The outcome of this calculation is a transformer with 11 turns, 3 cores, and a switching frequency of $180.4\,\mathrm{kHz}$. The 3 experimental tests were replicated, and the full load waveforms are shown in Fig. 12.

| Nodal temperatures (°C) | | | | | |
|---|---|---|---|---|---|
| (1) Inner | (2) Top | (3) Outer | (4) Bottom | (5) Primary | (6) Secondary |
| 84.7 | 74.1 | 64.7 | 76.7 | 110.1 | 107.7 |

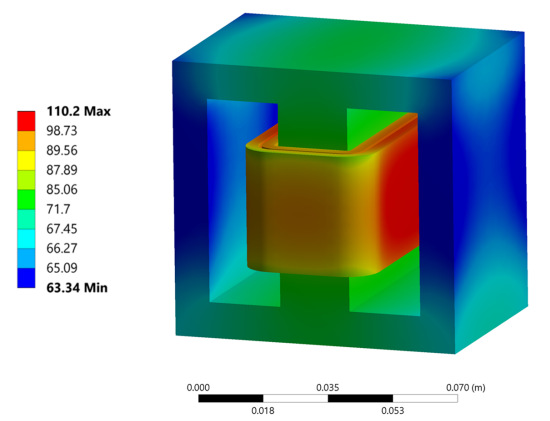


Fig. 14. Thermal FEA model results of ASM design and predicted nodal temperatures.

This experiment shows much better correlation with the analytical model. The core losses, now at $5.8\,\mathrm{W}$, are only $10\%$ error from the simulated core losses in one iteration. This single-step process has been found to occur with other applications of space mapping techniques [48]. The steady-state temperatures, fundamental to a functional transformer, follow the analytical thermal model temperatures. Vitally, the hot spot temperature at Node 1, the center core limb, matches the simulated value. This ensures that the steady-state temperature for the transformer is not underestimated and thereby avoids failure in long-term testing and reliability. The other nodal temperatures are reasonably estimated using the analytical model. Refer to Table II for these results and Fig. 13 for the physical build of the ASM design used for testing. The final efficiency is $99.53\%$, and the power density is $9\,\mathrm{kW/L}$.

In a similar manner to the SOA design, the estimations from FEA correlate to the loss and temperature measurements as shown in Fig. 14. The FEA model predicted the core hot spot as $84.7\,^{\circ}\mathrm{C}$ while the average temperature of the core was $74.5\,^{\circ}\mathrm{C}$.

### E. Comparison of Nominal Optimization Results

It is straightforward in Table II that the SOA experimental results are far from expected by the analytical model in terms of losses and steady-state temperatures. This is due to the limiting assumptions created by modeling physical behaviors [49]. However, it is possible to improve the thermal outcomes using this ASM technique to find a new design point which is accurately characterized through the analytical model via the space mapping shift at the core loss value. In comparing these two optimization methods, the trade-offs of each method should be discussed. By using the SOA method, the electrical requirements are the only ones which are satisfied. The mechanical requirements are not met since the estimated temperatures are not paralleled in the experimental results. However, the ASM method enables the integration of both electrical and mechanical designs to create a trade-off that accurately depicts both domains.

It is important to discuss the changes in the transformer design to achieve the final product. Of the three design variables, the number of cores, and thus core volume, remains unchanged. There is a small adjustment applied by increasing the number of turns by one which increases the total winding losses. It is also pertinent to discuss the change in leakage inductance due to the change in the number of turns. The SOA design hosted a $3.79\,\mu\mathrm{H}$ leakage inductance while the ASM build maintained $3.84\,\mu\mathrm{H}$. The minute $1\%$ difference in these values implies that using ASM does not affect the leakage inductance considerations while reducing modeling error. Thus, a leakage inductance requirement would be unaffected.

While the total losses have increased, shifting losses from the core to the windings reduces the steady-state temperatures of the transformer, most notably in the hot spot of Node 1 and the rest of the core. Though it may seem that the SOA method offers an optimum design point with higher efficiency, it is based on the incorrect assumption that temperature estimations are accurate, which has been proven to

TABLE II
COMPARISON OF OPTIMIZATION MODEL AND EXPERIMENTAL RESULTS

| | | Analytical Model | SOA Hardware | ASM Hardware |
|---|---|---|---|---|
| Design Variables | Number of Cores | 3 | 3 | 3 |
| | Turns | 10 | 10 | 11 |
| | Switching Frequency (kHz) | 187.5 | 187.5 | 180.4 |
| Losses (W) | Core Losses | **5.26** | 7.4 | 5.8 |
| | Primary Losses | 3.86 | 3.8 | 4.8 |
| | Secondary Losses | 4.17 | 4.3 | 5.7 |
| | **Total Losses** | 13.29 | 15.5 | 16.3 |
| Nodal Temperatures (°C) | (1) Center limb | **85** | 97.5 | 84.4 |
| | (2) Upper yoke | 64.5 | 84.4 | 72.5 |
| | (3) Outer limb | 62 | 69.8 | 57.8 |
| | (4) Lower yoke | 76.2 | 76.5 | 66.6 |
| | (5) Primary | 121.7 | 115 | 115 |
| | (6) Secondary | 118.8 | 108 | 109 |

be false. If unchecked, the underestimation of the hotspot temperature can be detrimental to the MFT and, ultimately, cause failure of the component. Therefore, ASM is beneficial to incorporate without adding impactful negative consequences for the final transformer design. While this process is more intensive than the SOA in terms of design and implementation, it is a formulated, iterative process that shifts the design using previously collected data. This removes the guesswork of iterative design changes that do not rely on such a process.

The winding temperatures are overestimated in the analytical model for two reasons. First, the windings are assumed to only emit heat in the horizontal direction of Fig. 3(a). Realistically, heat is transferred also in the vertical direction. Secondly, the contact resistances between the windings and the central core limb have been simplified to an air gap which leads to a higher thermal resistance. These reasonable assumptions enable a fast coarse model which can be adjusted for better accuracy with ASM. The assumption of a completely insulated bottom causes Node 4 to be inaccurate. However, this work also shows that inaccuracies made by assumptions in the coarse model can be overcome by the ASM technique in a single iteration of the ASM method.

### F. Thermal Influence on Practical Designs

The experiments were designed based on the assumption of thermal isolation for the MFT. However, this is not an acceptable assumption for practical applications. Therefore, an extension of the SOA experiment occurred to include MFT proximity to other components. In this experiment, an electrical insulation board of $0.125''$ thickness was placed $40\,\mathrm{mm}$ away from the upper yoke and $35\,\mathrm{mm}$ away from the outer limb of the core. These nodes were chosen based on the likelihood of component placement next to the MFT and to trap the rising heat from escaping to cause a worst-case scenario. Table III shows the minute changes over the course of $30\,\mathrm{min}$ in the core nodal temperatures with this change. The first row at $180\,\mathrm{min}$ shows the initial steady-state temperatures before the addition of the board. These results show that lower loss, nearby components in converter design may not affect the MFT optimization procedure. More research is needed to understand how and at what temperature heat generating components can affect an MFT, beyond higher enclosure ambient temperature.

TABLE III
EXPERIMENT ON THERMAL CONSIDERATIONS OF PRACTICAL DESIGN

| Time (min) | (1) Center limb (°C) | (2) Upper yoke (°C) | (3) Outer limb (°C) | (4) Lower yoke (°C) |
|---|---|---|---|---|
| 180 | 97.5 | 84.4 | 69.8 | 76.5 |
| 195 | 97.7 | 86.3 | 69.5 | 76.8 |
| 210 | 97.6 | 86.6 | 70.6 | 76.8 |

## V. ROBUST OPTIMIZATION

The nominal optimization routines previously described are best for single-build setups that occur in research facilities. ASM enables high efficiency and power density while incorporating accurate temperature estimations. However, close proximity to active constraints leads to the possibility of infeasible experimental results. This section aims to incorporate a well-known optimization technique to avoid infeasible designs by moving the optimal design away from active constraints that may be violated due to tolerances in the design.

Unlike Section IV, robust optimization does not rely solely on a nominally optimized algorithm. Therefore, the variations in the optimal design can be shown and integrated into the optimization routine for mass production with low numbers of defective products. This differs from ASM optimization as ASM is better suited for small-scale production.

### A. Robust Optimization Methodology

Differences between the simulated and physical results are considered to be expected. However, this research seeks to examine the variations to a further degree than has been done before with MFTs. The technique of robust optimization enables this analysis. First, the robust optimization algorithm is defined. Then, the variances that create the differences in the analytical model and experimental results are calculated. This step enables a deeper understanding of overall MFT variation, and the outcomes are probed thoroughly in Section V-B. Finally, this MFT design is robustly optimized. Statistical tolerances were used in this optimization technique since a

collection of tolerances to create the worst-case design is unlikely.

There is a simple process to follow to create a robust design with statistical tolerances:

1) Solve the nominal optimization process as previously completed in Section IV-A,
2) Calculate the transmitted variation,
3) Adjust the constraints by the amount of transmitted variation, and
4) Re-optimize to find the robust optimization.

The assumptions to this method are:

- The transmitted variance is constant in the design space,
- The robust optimum is near the nominal optimum,
- The derivatives are constant,
- Constraints have a normal distribution, and
- Constraints are independent.

Following the methodology in [32], the generic optimization problem, updated from Section IV, is

$$\begin{aligned} &\text{Min} \quad f(\mathbf{x}, \mathbf{p}) \\ &\text{s.t.} \quad g_i(\mathbf{x}, \mathbf{p}) \leq b_i \quad i = 1, \ldots, m \end{aligned} \tag{35}$$

where $\mathbf{x}$ is an $n$ dimensional vector of design variables, and $\mathbf{p}$ is an $l$ dimensional vector of constant parameters. In the case of the MFT, $\mathbf{x}$ is the array of the design variables, the number of windings and cores and the switching frequency. The variable $\mathbf{p}$ includes any parameters that are not design variables but have tolerances. For the nominal values of $\mathbf{x}$, $\mathbf{p}$, and $\mathbf{b}$, deviations, $\Delta\mathbf{x}$, $\Delta\mathbf{p}$, and $\Delta\mathbf{b}$, can occur. To mitigate the effects due to these fluctuations, the size of the feasible region is appropriately reduced. In this instance, the nominal optimization method (without any tolerances) was defined in Section IV-A, and this section is the means to extend the optimization algorithm to account for variations that may occur in the MFT.

To avoid the overly-conservative worst-case analysis, deviations are considered as independent random variables, and the likelihood of all worst-cases happening simultaneously is rare. Therefore, statistical tolerances are used to handle this low probability of occurrence. The statistical variance is estimated by a first order Taylor series to be

$$\sigma_{g_i}^2 = \sum_{j=1}^{n} \left( \frac{\delta g_i}{\delta x_j} \sigma_{x_j} \right)^2 + \sum_{j=1}^{l} \left( \frac{\delta g_i}{\delta p_j} \sigma_{p_j} \right)^2. \tag{36}$$

The mean is the nominal value of the parameter being varied, and the standard deviation, $\sigma$, is the square root of the variance. The total constraint variance is

$$\sigma_i^2 = \sigma_{b_i}^2 + \sigma_{g_i}^2. \tag{37}$$

The constraints can be modified to handle the transmitted variance using

$$g_i \leq b_i - k\sigma_i \tag{38}$$

where $k$ is the number of standard deviations selected to shift the constraint. The level of feasibility is given in Table IV for different values of $k$. Based on the percentage of feasible designs, $k$ is chosen to be 2 for this robust optimization. To convey the magnitude of variation due to individual tolerances, $\sigma_{g_{i,p_j}}^2$ is defined as

$$\sigma_{g_{i,p_j}}^2 = \frac{\delta g_i}{\delta p_j} \sigma_{p_j}^2. \tag{39}$$

TABLE IV
RELATION OF $k$ TO DESIGN FEASIBILITY

| $k$ Value | Percentage of Designs within $k\sigma$ |
|---|---|
| 1 | 84.13% |
| 2 | 97.725% |
| 3 | 99.865% |
| 4 | 99.9968% |

### B. Sensitivity Analysis

In monitoring the differences between the analytical model and experimentation, it is important to recognize the impacts of variations that can occur in the MFT hardware. While [50], [51] attempts to show this variation, it is only shown in comparison of the modeled design and the singular hardware implementation. This work is directed at all potential deviations that can occur, for example, in large-scale manufacturing. These variations may cause unwanted behaviors in the system that can influence the experimental results. There are two categories of variability that can occur in hardware. First, there are system-level attributes, such as closed-loop controls, which can affect power loss of the MFT. Second, manufacturing tolerances of the cores or the winding length per turn exist which are outside of the system or researcher control.

Figure 15 depicts the affects of both these variabilities based on a single set of design variables within a reasonable variation of each parameter individually. These values are chosen based on data from existing literature and generic converter design requirements [2], [50]. Changes to these variations should be made depending on the requirements for a specific system as needed. The parameter tolerances, $\Delta\mathbf{p}$, are identified in Table V. The percentages denote the variation in terms of the nominal design point. Variations in the design variables are also incorporated in this table. The core volume tolerance is per unit to the number of cores, and the $MLT$ is varied for each turn of winding. The switching frequency tolerance is embedded within current, voltage, and core loss tolerances.

Deviations in core loss, turns ratio, $MLT$, core volume, and cross-sectional area are due to manufacturing tolerances.

TABLE V
PARAMETER TOLERANCES

| **Parameter, p** | **Tolerance, $\Delta$p** |
|---|---|
| Primary Current, $I_{pri}$ | $\pm$10% |
| Ambient Temperature, $T_{amb}$ | +30°C |
| Duty Cycle, $D$ | -0.08 |
| Primary Voltage, $V_{pri}$ | $\pm$5% |
| Core Loss, $P_c$ | $\pm$20% |
| Turns Ratio, $N_{ratio}$ | $\pm$2% |
| Length per Turn, $MLT$ | $\pm$10% |
| Core Volume, $V_{core}$ | $\pm$3.33E-6 m$^3$ |
| Cross-sectional Area, $A_c$ | $\pm$1.6E-5 m$^2$ |

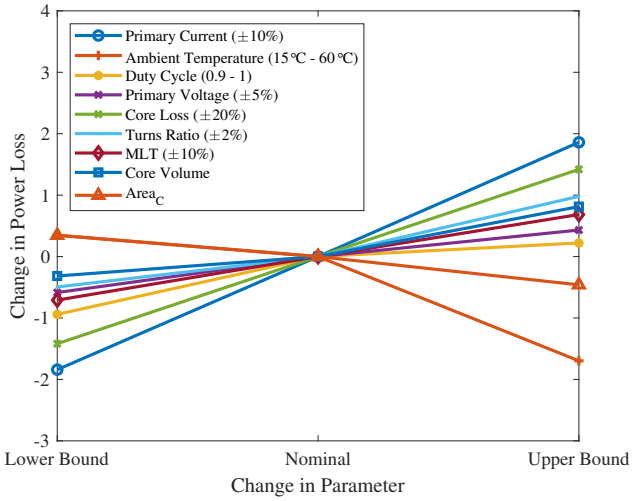


Fig. 15. Sensitivity analysis of MFT.

The latter two are based on the tolerances provided in the datasheet. The other parameters are based on the system-level traits. Variation is disclosed by the overall slope of the line of each between the lower bound and higher bound tolerances. Straighter horizontal lines depict less variation than ones with larger changes in power loss. This figure shows that the largest variations stem from changes in primary current, ambient temperature, and core loss.

These large sensitivities are intuitive. Copper loss is dependent on the square of the current in the windings. The iterative nature of temperature and core loss where the ambient temperature is the ground of the thermal resistive network suggests the necessity to accurately predict the ambient temperature near the MFT. Lastly, the core losses are a well-known issue. Variation can occur both in the manufactured products and the equations used to predict losses. The coefficients used in the iGSE model are generally based on measurements taken using sinusoidal waveforms provided by the manufacturer. A typical, but time-consuming, method to avoid core loss discrepancies is to self-characterize the core material [52]. However, this method only reduces one of many points of variability. It does not do enough to reduce the discrepancy on its own. These other tolerances also need to be monitored.

### C. Statistical Variances and Observations

*1) Variances in the Constraints:* There are 8 constraints of concern in this optimization algorithm:

$$50\,\mathrm{mT} \leq B_m \leq 200\,\mathrm{mT} \text{ and} \tag{40}$$

$$\mathbf{T} = T_{amb} + \Delta\mathbf{T} \leq \mathbf{T}_{max}. \tag{41}$$

where $B_m$ is the peak flux density, $\mathbf{T}$ is the set of temperatures of the 6 thermal nodes denoted in Fig. 3, and $\mathbf{T}_{max}$ is 100 °C for the core and 120 °C for the windings. The active constraints are the minimum flux density and the winding temperatures. It should be noted that there is a convoluted relationship between the matrix $\Delta\mathbf{T}$ and $B_m$ through the core loss. Therefore, the core loss density, $p_{core}$, is considered a constant parameter

TABLE VI
CONSTRAINT VARIANCE BY INDIVIDUAL PARAMETER

| **Constraint,** $g_i$ | **Parameter, p** | $\sigma_{g_{i,p_j}}$ |
|---|---|---|
| Flux Density, $B_m$ | $V_{pri}$ | 2.5E-3 |
| | $D$ | 2.46E-3 |
| | $A_c$ | 2.04E-3 |
| Center Limb, $T_1$ | $T_{amb}$ | 18.08 |
| | $I_{pri}$ | 5.52 |
| | $P_c$ | 1.52 |
| | $V_{core}$ | 3.7E-10 |
| Upper Yoke, $T_2$ | $T_{amb}$ | 18.08 |
| | $P_c$ | 5.86 |
| | $V_{core}$ | 0.034 |
| Outer Limb, $T_3$ | $T_{amb}$ | 18.08 |
| | $P_c$ | 4.85 |
| | $V_{core}$ | 2E-9 |
| Lower Yoke, $T_4$ | $T_{amb}$ | 18.08 |
| | $P_c$ | 5.72 |
| | $V_{core}$ | 4E-9 |
| Primary Winding, $T_5$ | $T_{amb}$ | 18.08 |
| | $P_c$ | 3.25 |
| | $I_{pri}$ | 2.87 |
| | $N_{ratio}$ | 1.47 |
| | $V_{core}$ | 2E-9 |
| Secondary Winding, $T_6$ | $T_{amb}$ | 18.08 |
| | $I_{pri}$ | 5.97 |
| | $N_{ratio}$ | 0.138 |

to avoid interdependence of the constraints in the statistical analysis. This also aids to identify discrepancies when the core loss measured is different from the estimated core loss from the analytical model or from the expected value given by the manufacturer. Following the method described in Section V-A, the constraint variations can be calculated at the optimized design point.

Table VI shows the individual variances for each constraint in order of magnitude, and Table VII describes the total variance for each constraint considering all parameter variances. It can be seen that the variance is equally, and minimally, influenced by the duty cycle, primary voltage, and cross-sectional area for the flux density.

The temperature matrix has an average standard deviation of 18.9 °C, an average of 22%. This shows that the highest potential for infeasibility stems from the thermal requirements. The largest variation in the temperature constraint stems from the ambient temperature. If this is not properly identified, the design is likely to be infeasible. However, ambient temperatures can vary widely from initial designs to final experimental hardware due to nearby heat generation, additions of enclosures, and seasonal changes.

TABLE VII
TOTAL CONSTRAINT VARIANCES

| **Constraint,** $g_i$ | $\sigma_{g_i}$ |
|---|---|
| $B_m$ | 5.23E-03 |
| $T_1$ | 18.97 |
| $T_2$ | 19.01 |
| $T_3$ | 18.72 |
| $T_4$ | 18.97 |
| $T_5$ | 18.60 |
| $T_6$ | 19.04 |

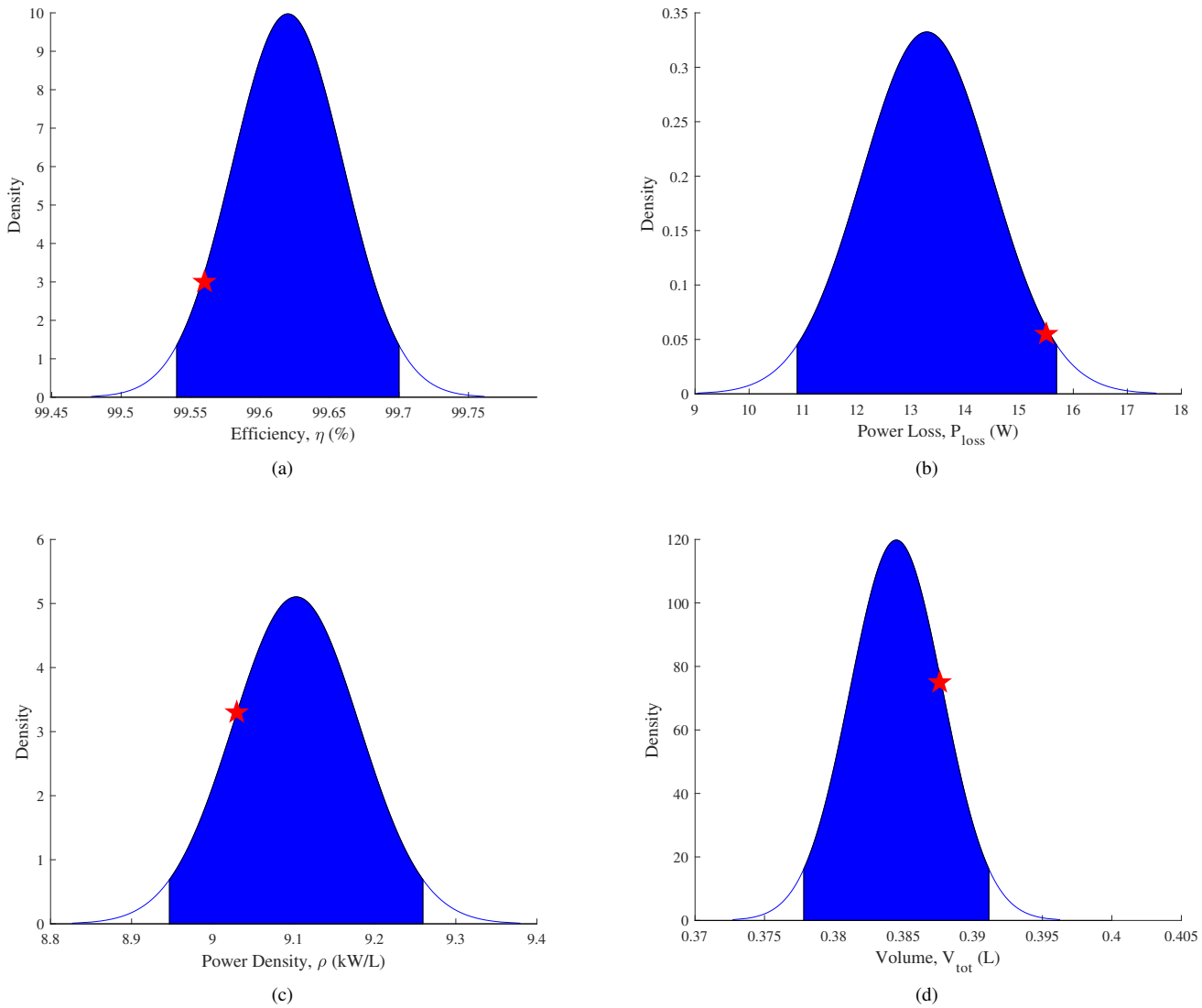


Fig. 16. Normal distribution of potential designs versus (a) efficiency , (b) power loss, (c) power density, and (d) volume. The shaded area depicts 97.725% of potential designs due to tolerances, and the red star is the experimental result.

For the temperatures at the center limb, the primary winding, and the secondary winding, the next influential parameter is the primary current. This is due to the thermal resistive network connections between the primary winding to the inner core volume and to the secondary winding. Compared to these parameters, the core loss density and the core volume are insignificant in terms of variation. However, the core loss density is as influential for the rest of the core as the primary current at the center limb of the E-core.

If the ambient temperature is considered to have smaller variation, it can reduce the variance in the thermal constraints greatly until another parameter's variance becomes larger than the ambient temperature variance. For example, a tolerance of $10\,^{\circ}\mathrm{C}$ can reduce this to an average standard deviation of $8.1\,^{\circ}\mathrm{C}$, or the variance at $20\,^{\circ}\mathrm{C}$ is less than $13.5\,^{\circ}\mathrm{C}$. Below $10\,^{\circ}\mathrm{C}$ variation, the primary current variation dominates. Therefore, it is recommended that the ambient temperature is within a $10\,^{\circ}\mathrm{C}$ estimation, when possible, to reduce the potential deviations in the design.

*2) Variances in the Objectives:* By replacing the constraints with the objective functions, efficiency, $\eta$, and power density, $\rho$, some interesting correlations can be made. Table VIII shows the individual variance for each parameter as it relates to efficiency and total power loss, $P_{loss}$. To simplify the relationships, the total power loss and volume are used as modified objective functions. It can be seen that the largest variance stems from core loss density for power loss. Considering power density, and thus volume, the only variance comes from the change in core volume. This is assuming that the majority of the total volume is due to the cores. This is reasonable since there is a low likelihood of the windings being wound loosely enough to greatly influence the volume with a shell-type transformer.

The total objective variances can be seen in Table IX. The efficiency and power loss are affected more than power density and volume. This is in accordance with the previous data.

TABLE VIII
OBJECTIVE VARIANCE BY INDIVIDUAL PARAMETER

| Objective | Parameter, p | $\sigma_{F_{i,p_j}}$ |
|---|---|---|
| $\eta$ | $P_c$ | 0.029 |
| | $I_{pri}$ | 0.017 |
| | $V_{core}$ | 2.3E-3 |
| | $MLT$ | 1.9E-3 |
| $P_{loss}$ | $P_c$ | 1.03 |
| | $I_{pri}$ | 0.6 |
| | $V_{core}$ | 0.08 |
| | $MLT$ | 0.066 |

Therefore, the comparison between the nominally optimized MFT and the deviation in the experimental results can be made. This is done by allowing $2\sigma_\eta = \Delta\eta$, and the change in $\eta$ is $\eta \pm \Delta\eta$ for the change in efficiency. The same is done to power density, $\rho$. By plotting the normal distribution of the efficiency, total loss, power density, and volume in Fig. 16, the SOA experimental results are within $2\sigma$ of the nominal values for all the objectives. This means that the hardware from Section IV-B is within the design tolerance predicted. However, this shows that some potential designs could be infeasible. For example, the peak experimental core temperature was near $100\,^{\circ}\mathrm{C}$ due to the increased losses. Since this was an optimization constraint of the core, any design pushing this bound would be outside the feasible design space.

### D. Robust Optimization Results

In summation of the previous results, a robust optimization algorithm can be implemented for this MFT design. The temperature variation is limited to $10\,^{\circ}\mathrm{C}$, but all other tolerances are consistent with Table V. The constraint variation, in (38), was used to modify the nominal optimization method and convert the algorithm to a robust optimization.

Using the same design specifications from Section II, the results of this robust optimization procedure are given in Fig. 17. The highlighted regions maintain $2\sigma$ variation in both objectives. Assuming that the robustly optimized design is close to the originally optimized point, the same standard deviation variations apply to the new design point. This assumption holds true even though the number of cores has increased by one as the shift in power density describes. Therefore, the robustly optimized designs have increased in volume to adjust for the increased thermal restrictions. The highlighted design within the robust design region is a 10-turn, 4-core transformer with a switching frequency of $140.6\,\mathrm{kHz}$.

There exists a trade-off when using robust optimization versus nominal optimization. With this robust design, the volume, weight, losses, and costs have increased. However,

TABLE IX
TOTAL OBJECTIVE VARIANCES

| Objective | $\sigma_{F_i}$ |
|---|---|
| Efficiency, $\eta$ | 0.04 |
| Total Losses, $P_{loss}$ | 1.2 |
| Power Density, $\rho$ | 8.93E-2 |
| Total Volume, $V_{tot}$ | 3.33E-3 |

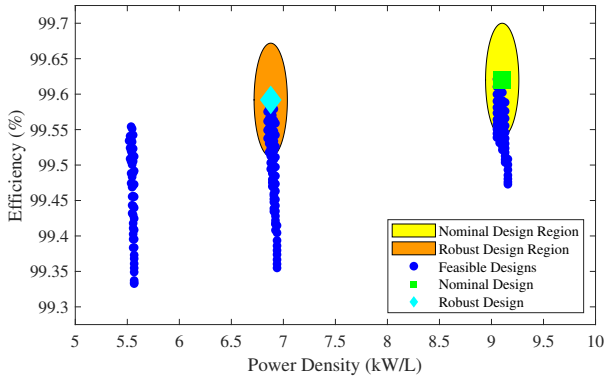


Fig. 17. Results of robust optimization of MFT design.

the number of rejected parts would be reduced in a large manufacturing setting. This enables high quality control while optimizing the design as much as possible.

Another key factor of concern is the change in leakage inductance from the nominally optimized MFT. The robustly optimized MFT has a calculated leakage inductance of 3.93 uH. This is a 3.6% difference from the 3.79 uH leakage inductance of the nominal design and should be well within the bounds of the acceptable leakage inductance range developed for specific converter applications. If there is a specific range for the leakage inductance, it can always be added as constraints to the method [14]

## VI. CONCLUSION

This paper has proposed a unique method to improve the comparison of transformer optimization and physical implementation using Aggressive Space Mapping using experimental results. A State of the Art optimization method is used to find an optimal transformer design. The data from the SOA experimental results are used to find a new ASM design that aligns with the original goals and outcomes of the analytical model. This design method has been shown to implement an optimized transformer by estimating the hot spot temperatures accurately to achieve a reliable, feasible, and realistic MFT. This outcome occurs with only one redesign, or iteration of ASM. This method can be used for any MFT turns ratio since only one winding is considered a design variable.

This work has also shown the influence of parametric uncertainty on the MFT hardware. This is done by first understanding from where potential deviations of constant parameters arise. By using sensitivity analysis, the influence of each parameter on the objectives was observed and a potential region for product variation was defined which contained 97.725% of all design variations. As predicted by the design region, the hardware of this design point has been shown to fall within $2\sigma$ of the nominal design. This verifies the need to quantify the variation in MFT designs and necessitates robust optimization. Finally, the robust optimization procedure was evaluated to show the shift from the nominally optimized design to the updated design region.

ASM and robust optimization are valuable tools for pushing the boundaries of power density and efficiency for MFT

design in a specific application. As with any tool, it is vital that these algorithms are used in the method that is most advantageous for the engineer. Small-scale production is greatly enhanced by ASM techniques while mass production receives valuable insight using robust optimization. While this work was specifically focused on the MFT optimization, future accommodations will be necessary to build a full converter-level optimization, including semiconductor requirements.

As future work, more design variables and constraints will be added to this optimization method. The purpose of this small-scale study is to display these valuable optimization methods to the MFT design process. As this research continues, we expect to add more variables to the process, including core structures, core materials, winding sizes and types, cooling methods, voltage isolation constraints, and physical winding layouts to provide opportunities for wider application.

## REFERENCES


[1] Y. Sun, Z. Gao, C. Fu, C. Wu, and Z. Chen, "A hybrid modular DC Solid-State transformer combining high efficiency and control flexibility," *IEEE Trans. Power Electron.*, vol. 35, no. 4, pp. 3434–3449, Apr. 2020.

[2] Q. Zhu, L. Wang, A. Q. Huang, K. Booth, and L. Zhang, "7.2-kv Single-Stage Solid-State transformer based on the Current-Fed series resonant converter and 15-kv SiC mosfets," *IEEE Trans. Power Electron.*, vol. 34, no. 2, pp. 1099–1112, Feb. 2019.

[3] M. J. Mauger, P. Kandula, and D. Divan, "Optimal design of the resonant tank of the Soft-Switching Solid-State transformer," in *2019 IEEE Energy Conversion Congress and Exposition (ECCE)*, Sep. 2019, pp. 6965–6972.

[4] X. She, A. Q. Huang, and R. Burgos, "Review of Solid-State transformer technologies and their application in power distribution systems," *IEEE Journal of Emerging and Selected Topics in Power Electronics*, vol. 1, no. 3, pp. 186–198, 2013.

[5] J. E. Huber, J. Böhler, D. Rothmund, and J. W. Kolar, "Analysis and cell-level experimental verification of a 25 kw all-SiC isolated front end 6.6 kv/400 V AC-DC solid-state transformer," *CPSS Transactions on Power Electronics and Applications*, vol. 2, no. 2, pp. 140–148, 2017.

[6] T. O. Olowu, H. Jafari, M. Moghaddami, and A. I. Sarwat, "Physics-Based design optimization of high frequency transformers for solid state transformer applications," in *2019 IEEE Industry Applications Society Annual Meeting*, Sep. 2019, pp. 1–6.

[7] J. Feng, W. Q. Chu, Z. Zhang, and Z. Q. Zhu, "Power electronic Transformer-Based railway traction systems: Challenges and opportunities," *IEEE Journal of Emerging and Selected Topics in Power Electronics*, vol. 5, no. 3, pp. 1237–1253, 2017.

[8] Y. Shen, H. Wang, A. Al-Durra, Z. Qin, and F. Blaabjerg, "A bidirectional resonant DC–DC converter suitable for wide voltage gain range," *IEEE Trans. Power Electron.*, vol. 33, no. 4, pp. 2957–2975, Apr. 2018.

[9] S. Srdic, X. Liang, C. Zhang, W. Yu, and S. Lukic, "A SiC-based high-performance medium-voltage fast charger for plug-in electric vehicles," in *2016 IEEE Energy Conversion Congress and Exposition (ECCE)*, 2016, pp. 1–6.

[10] X. Liang, S. Srdic, J. Won, E. Aponte, K. Booth, and S. Lukic, "A 12.47 kv medium voltage input 350 kw EV fast charger using 10 kv SiC MOSFET," in *2019 IEEE Applied Power Electronics Conference and Exposition (APEC)*, Mar. 2019, pp. 581–587.

[11] S. Zou, J. Lu, A. Mallik, and A. Khaligh, "Modeling and optimization of an integrated transformer for electric vehicle On-Board charger applications," *IEEE Transactions on Transportation Electrification*, vol. 4, no. 2, pp. 355–363, Jun. 2018.

[12] M. A. Bahmani, T. Thiringer, and M. Kharezy, "Design methodology and optimization of a medium frequency transformer for high power DC-DC applications," in *2015 IEEE Applied Power Electronics Conference and Exposition (APEC)*, Mar. 2015, pp. 2532–2539.

[13] M. Mogorovic and D. Dujic, "100kw, 10khz medium frequency transformer design optimization and experimental verification," *IEEE Trans. Power Electron.*, pp. 1–1, 2018.

[14] A. Garcia-Bediaga, I. Villar, A. Rujas, L. Mir, and A. Rufer, "Multi-objective optimization of Medium-Frequency transformers for isolated Soft-Switching converters using a genetic algorithm," *IEEE Trans. Power Electron.*, vol. 32, no. 4, pp. 2995–3006, Apr. 2017.

[15] M. Mogorovic and D. Dujic, "Thermal modeling and experimental verification of an air cooled medium frequency transformer," in *2017 19th European Conference on Power Electronics and Applications (EPE'17 ECCE Europe)*, Sep. 2017, pp. P.1–P.9.

[16] M. A. Bahmani, T. Thiringer, and M. Kharezy, "Design methodology and optimization of a Medium-Frequency transformer for High-Power DC-DC applications," *IEEE Trans. Ind. Appl.*, vol. 52, no. 5, pp. 4225–4233, 2016.

[17] S. D. Sudhoff, *Power Magnetic Devices: A Multi-Objective Design Approach*. John Wiley & Sons, Jan. 2014.

[18] P. Shuai and J. Biela, "Design and optimization of medium frequency, medium voltage transformers," in *2013 15th European Conference on Power Electronics and Applications (EPE)*, 2013, pp. 1–10.

[19] M. S. Mohammed and R. A. Vural, "NSGA-II+FEM based loss optimization of Three-Phase transformer," *IEEE Trans. Ind. Electron.*, vol. 66, no. 9, pp. 7417–7425, Sep. 2019.

[20] B. Sun, R. Burgos, and D. Boroyevich, "Modeling and optimization of High-Frequency Litz-Wire transformer for 10 kw GaN-Based LLC resonant converter," in *2018 IEEE 19th Workshop on Control and Modeling for Power Electronics (COMPEL)*, Jun. 2018, pp. 1–7.

[21] X. Yu, J. Su, J. Lai, and S. Guo, "Analytical optimization of Non-Saturated thermally limited High-Frequency Transformer/Inductor design considering discreteness of design variables," *IEEE Trans. Power Electron.*, pp. 1–1, 2019.

[22] R. B. Ayed, J. Gong, S. Brisset, F. Gillon, and P. Brochet, "Three-Level output space mapping strategy for electromagnetic design optimization," *IEEE Trans. Magn.*, vol. 48, no. 2, pp. 671–674, Feb. 2012.

[23] S. Candolfi, P. Viarouge, D. Aguglia, and J. Cros, "Hybrid design optimization of high voltage pulse transformers for klystron modulators," *IEEE Trans. Dielectr. Electr. Insul.*, vol. 22, no. 6, pp. 3617–3624, Dec. 2015.

[24] A. C. Berbecea, R. Ben-Ayed, F. Gillon, S. Brisset, and P. Brisset, "Comparison of efficient global optimization and output space mapping on the biobjective optimization of a safety isolating transformer," *IEEE Trans. Magn.*, vol. 48, no. 2, pp. 791–794, Feb. 2012.

[25] J. Gong, F. Gillon, and N. Bracikowski, "Comparison of three space mapping techniques on electromagnetic design optimization," *COMPEL - The international journal for computation and mathematics in electrical and electronic engineering*, vol. 37, no. 2, pp. 565–580, 2018.

[26] R. Khlissa, S. Vivier, L. A. O. Vargas, and G. Friedrich, "Application of output space mapping method for fast optimization using multi-physical modeling," in *2012 IEEE Energy Conversion Congress and Exposition (ECCE)*, 2012, pp. 1306–1313.

[27] S. Vivier and G. Friedrich, "Comparison between Single-Model and multimodel optimization methods for multiphysical design of electrical machines," *IEEE Trans. Ind. Appl.*, vol. 54, no. 2, pp. 1379–1389, Mar. 2018.

[28] A. Parkinson, C. Sorensen, and N. Pourhassan, "A general approach for robust optimal design," *J. Mech. Des.*, vol. 115, no. 1, pp. 74–80, Mar. 1993.

[29] G. Emch and A. Parkinson, "Robust optimal design for Worst-Case tolerances," *J. Mech. Des.*, vol. 116, no. 4, pp. 1019–1025, Dec. 1994.

[30] W. Chen, J. K. Allen, K. L. Tsui, and F. Mistree, "A procedure for robust design: Minimizing variations caused by noise factors and control factors," *J. Mech. Des.*, vol. 118, no. 4, pp. 478–485, Jan. 1996.

[31] D. Bertsimas, D. B. Brown, and C. Caramanis, "Theory and applications of robust optimization," *SIAM Rev.*, vol. 53, no. 3, pp. 464–501, 2011.

[32] Parkinson, A.R., Balling, R., and J.D. Hedengren, "Robust design," in *Optimization Methods for Engineering Design*, Brigham Young University, Ed. Brigham Young University, 2013.

[33] K. Booth, H. Subramanyan, X. Liang, J. Liu, S. Srdic, and S. Lukic, "Optimization of medium frequency transformers with practical considerations," in *2019 IEEE Applied Power Electronics Conference and Exposition (APEC)*, Mar. 2019, pp. 2906–2911.

[34] M. Mogorovic and D. Dujic, "Medium frequency transformer leakage inductance modeling and experimental verification," in *2017 IEEE Energy Conversion Congress and Exposition (ECCE)*, Oct. 2017, pp. 419–424.

[35] "New England Wire," http://www.litzwire.com/nepdfs/Litz_Technical.pdf, accessed: 2018-02-15.

[36] P. L. Dowell, "Effects of eddy currents in transformer windings," *Electrical Engineers, Proceedings of the Institution of*, vol. 113, no. 8, pp. 1387–1394, Aug. 1966.

[37] R. Ridley, "Proximity loss in magnetics windings," 2005. [Online]. Available: http://www.ridleyengineering.com/design-center-ridley-engineering/49-circuit-designs/265-a22-magnetics-proximity-loss.html

[38] K. Venkatachalam, C. R. Sullivan, T. Abdallah, and H. Tacca, "Accurate prediction of ferrite core loss with nonsinusoidal waveforms using only steinmetz parameters," in *2002 IEEE Workshop on Computers in Power Electronics, 2002. Proceedings.*, Jun. 2002, pp. 36–41.

[39] "N87 datasheet," 2017. [Online]. Available: https://www.tdk-electronics.tdk.com/download/528882/71e02c7b9384de1331b3f625ce4b2123/pdf-n87.pdf

[40] T. L. Bergman, F. P. Incropera, D. P. DeWitt, and A. S. Lavine, *Fundamentals of heat and mass transfer*. John Wiley & Sons, 2011.

[41] H.-H. Lee, *Finite element simulations with ANSYS Workbench 18*. SDC publications, 2018.

[42] Y. Peng, "Research of thermal analysis collaboratively using ansys workbench and solidworks simulation," in *Applied Mechanics and Materials*, vol. 127. Trans Tech Publ, 2012, pp. 262–266.

[43] M. Leibl, G. Ortiz, and J. W. Kolar, "Design and experimental analysis of a Medium-Frequency transformer for Solid-State transformer applications," *IEEE Journal of Emerging and Selected Topics in Power Electronics*, vol. 5, no. 1, pp. 110–123, Mar. 2017.

[44] A. K. Das, Z. Wei, B. G. Fernandes, H. Tian, M. Thevar Shuyu, V. B. Sriram, A. Tripathi, and P. C. Kjær, "Multi-variable optimization methodology for medium-frequency high-power transformer design employing steepest descent method," in *APEC*, Mar. 2018, pp. 1786–1793.

[45] G. A. Hazelrigg, "A framework for Decision-Based engineering design," *J. Mech. Des.*, vol. 120, no. 4, pp. 653–658, Dec. 1998.

[46] J. W. Bandler, R. M. Biernacki, S. H. Chen, R. H. Hemmers, and K. Madsen, "Electromagnetic optimization exploiting aggressive space mapping," *IEEE Trans. Microw. Theory Tech.*, vol. 43, no. 12, pp. 2874–2882, Dec. 1995.

[47] J. W. Bandler, Q. S. Cheng, S. A. Dakroury, A. S. Mohamed, M. H. Bakr, K. Madsen, and J. Sondergaard, "Space mapping: the state of the art," *IEEE Trans. Microw. Theory Tech.*, vol. 52, no. 1, pp. 337–361, Jan. 2004.

[48] J. Ossorio, J. C. Melgarejo, V. E. Boria, M. Guglielmi, and J. W. Bandler, "On the alignment of Low-Fidelity and high- fidelity simulation spaces for the design of microwave waveguide filters," *IEEE Trans. Microw. Theory Tech.*, vol. 66, no. 12, pp. 5183–5196, Dec. 2018.

[49] K. Booth and J. Bandler, "Space mapping for codesigned magnetics: Optimization techniques for high-fidelity multidomain design specifications," *IEEE Power Electronics Magazine*, vol. 7, no. 2, pp. 47–52, 2020.

[50] M. Mogorovic and D. Dujic, "Sensitivity analysis of medium frequency transformer design," in *2018 International Power Electronics Conference (IPEC-Niigata 2018 -ECCE Asia)*, May 2018, pp. 2170–2175.

[51] M. Mogorovic and D. Dujic, "Sensitivity analysis of Medium-Frequency transformer designs for Solid-State transformers," *IEEE Trans. Power Electron.*, vol. 34, no. 9, pp. 8356–8367, Sep. 2019.

[52] R. M. Burkart, "Advanced modeling and Multi-Objective optimization of power electronic converter systems," Ph.D. dissertation, ETH Zurich, 2016.